

# Dense dark-bright soliton arrays in a two-component Bose-Einstein condensate

S. Mossman,<sup>1</sup> G. C. Katsimiga,<sup>2,3</sup> S. I. Mistakidis,<sup>4,5</sup> A. Romero-Ros,<sup>3</sup>  
T. M. Bersano,<sup>1</sup> P. Schmelcher,<sup>3,6</sup> P. G. Kevrekidis,<sup>2</sup> and P. Engels<sup>1,\*</sup>

<sup>1</sup>*Department of Physics and Astronomy, Washington State University, Pullman, Washington 99164-2814*

<sup>2</sup>*Department of Mathematics and Statistics, University of Massachusetts, Amherst MA 01003-4515*

<sup>3</sup>*Center for Optical Quantum Technologies, Department of Physics,*

*University of Hamburg, Luruper Chaussee 149, 22761 Hamburg, Germany*

<sup>4</sup>*ITAMP, Center for Astrophysics | Harvard & Smithsonian, Cambridge, MA 02138 USA*

<sup>5</sup>*Department of Physics, Harvard University, Cambridge, Massachusetts 02138, USA*

<sup>6</sup>*The Hamburg Centre for Ultrafast Imaging, University of Hamburg,  
Luruper Chaussee 149, 22761 Hamburg, Germany*

We present a combined experimental and theoretical study of regular dark-bright soliton arrays in a two-component atomic Bose-Einstein condensate. We demonstrate a microwave pulse-based winding technique which allows for a tunable number of solitary waves en route to observing their dynamics, quantified through Fourier analysis of the density. We characterize different winding density regimes by the observed dynamics including the decay and revival of the Fourier peaks, the emergence of dark-antidark solitons, and disordering of the soliton array. The experimental results are in good agreement with three-dimensional numerical computations of the underlying mean-field theory. These observations open a window into the study of soliton crystals and the dynamics, excitations, and lifetimes of such patterns.

**Introduction.** Since their first observation in water waves [1, 2], the dynamics of solitary wave structures and patterns has evolved into a major thrust within nonlinear science. These dispersionless, localized, coherent structures, which can undergo collisions without changing shape, are found in a wide range of integrable and near-integrable systems with broad applicability in optics [3], atomic physics [4], plasmas [5], fluids [6] and other fields [6, 7]. For example, in nonlinear optics, solitons are considered as means for information transport through optical fibers [3], while in the context of matter waves, they have been argued as being relevant toward future matter-wave interferometers [4, 8, 9].

Dilute gas Bose-Einstein condensates (BECs) [8, 9] offer a highly flexible and controllable platform towards investigating the nonlinear dynamics and interactions of such solitary wave structures [4]. The relevant states range from dark [10] and bright [11] solitons in one-dimension (1D), and vortices [12] in two-dimensions, to several more exotic structures, including vortex lines and rings in three-dimensions (3D) [13]. In all of these settings, the universal interplay between dispersion and nonlinearity is responsible for the emergence and persistence of the relevant coherent structures [4].

In addition to the single-component wave structures mentioned above [4, 8, 9], the experimental realization of multi-component BECs [14, 15] has provided a substantial additional wealth of nonlinear states, including dark-bright (DB), dark-dark, as well as dark-antidark vector solitons, among many others summarized, e.g., in Ref. [16]. Recently, more complex soliton compounds were experimentally realized and studied in spinor BECs, such as three-component dark-dark-bright and dark-bright-bright solitons [17], the generation and

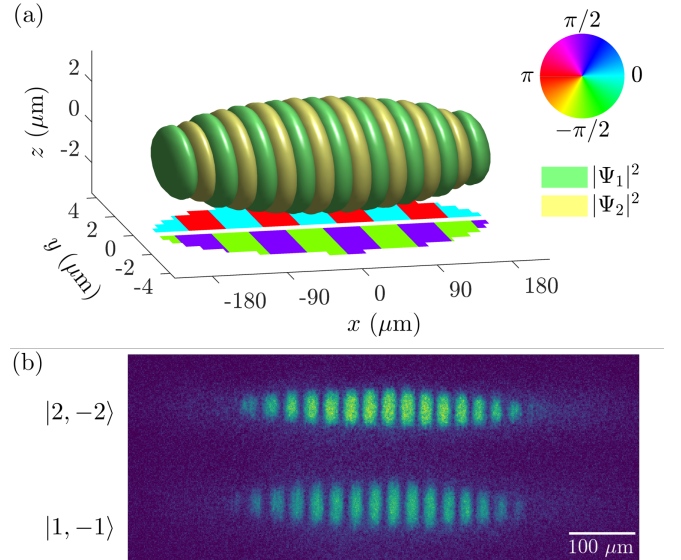


FIG. 1. (a) Example of a numerical initial configuration of the two-component elongated BEC. On the  $x$ - $y$  plane the condensate phase pattern corresponding to the  $|2, -2\rangle$  ( $|1, -1\rangle$ ) state is projected along the negative (positive)  $y$ -axis. (b) Example absorption image of the wound configuration after a winding time of  $\tau = 40$  ms with the  $|2, -2\rangle$  (top) and  $|1, -1\rangle$  (bottom) states imaged separately during time of flight.

collision of such structures [18], the creation of magnetic solitons [19, 20], as well as the proposal of twisted variants thereof [21]. While these structures merely represent a small fraction of recent experimental and theoretical developments, they reflect the extensive and broad interest and timeliness of this theme.

Despite the intense research efforts directed towards solitons and their dynamics, most of the associated ex-

perimental BEC studies have so far concentrated on individual solitons or very small clusters (or molecules) thereof [22] and their interactions [18]. However, over the past few years there has been a substantial interest towards the realization and exploration of soliton gases, given their intriguing generalized hydrodynamic properties [23]. The first experimental evidence for the realization of a soliton gas was obtained in hydrodynamics [24], while recently the relevant theory for integrable systems has been summarized in [25]. These investigations, along with earlier efforts (namely, on light pulses in optical fiber ring resonators [26]) and also ones in soliton turbulence in shallow water waves [27] usher us into a new era of soliton lattices, soliton fluids, and gases, as well as transitions between them [28].

In this letter, we present a combined experimental and numerical study of tightly packed DB soliton arrays in a two-component BEC. The soliton arrays generated in our experiments are large enough to be analyzed using spectral methods, fully tunable in the packing density of solitons, and are sufficiently long-lived to allow us to conduct detailed investigations of their dynamics. As a key result, we demonstrate the existence of three distinct dynamical regimes depending on the initial line density of solitons which we refer to as underwound, optimally wound, and overwound. These regimes are delineated by their length scale in relation to the natural soliton length scale as determined empirically from past realizations of DB solitons in this apparatus [17, 22, 29, 30]. The underwound regime is characterized by the spontaneous emergence and dynamic oscillation of dark-antidark solitons followed by apparent period doubling of the periodic array; the optimally wound configuration most closely matches the natural soliton length scale allowing for a more stable configuration which undergoes decay and revival of the soliton array; lastly, the overwound case pushes the limits of densely packed solitons giving way to long wavelength noise and disordered dynamics. We characterize the time dynamics in each regime through Fourier analysis of the atomic density and describe the qualitative nature of the solitonic features.

**Experimental Methods.** Our experimental technique for the generation of dense DB soliton arrays is based on a two-pulse Ramsey sequence in the presence of a small magnetic gradient. We begin with elongated BECs of approximately  $7 \times 10^5$   $^{87}\text{Rb}$  atoms in the  $|F, m_F\rangle = |1, -1\rangle$  hyperfine state held in an optical trap with harmonic trap frequencies of  $\omega/2\pi = \{3.06, 267, 278\}$  Hz. In the presence of a 10 G magnetic bias field, a fast microwave pulse is applied to coherently create an equal superposition of atoms in the  $|1, -1\rangle$  state and the  $|2, -2\rangle$  state. During a subsequent wait time, referred to as the winding time  $\tau$ , a slight gradient in the magnitude of the 10 G bias field along the long axis of the BEC leads to an accumulation of a linear phase gradient between the spin components. After the winding time, a second  $\pi/2$  pulse is applied

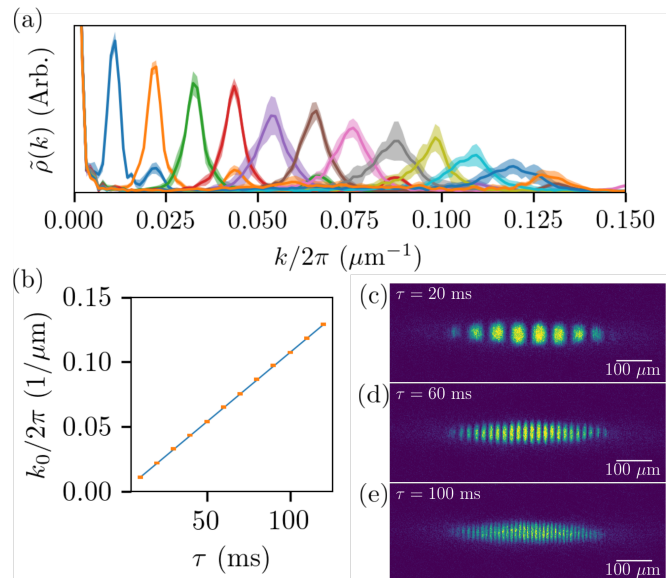


FIG. 2. (a) Experimental Fourier spectra for a range of winding times from  $\tau = 10$  ms to  $\tau = 120$  ms in steps of 10 ms. The  $k$ -vector of the corresponding fundamental peak  $k_0$  increases monotonically with  $\tau$ . Each spectrum is averaged over ten experimental realizations for a given winding time. The standard deviation in the averaged spectra is shown as a shaded region around each curve. (b) The center value wavenumber from fits to the peaks in panel (a). The standard error in each fit is smaller than the size of the markers. A linear fit indicates a winding rate of  $1.074(2) (\mu\text{m s})^{-1}$ . (c)–(e) Absorption images of the wound configuration after  $\tau = 20, 60$  and  $100$  ms of winding, respectively.

which, depending on the phase between the precessing spins and the microwave pulse, transfers atoms into the  $|2, -2\rangle$  state or back into the  $|1, -1\rangle$  state. This process produces a sinusoidal magnetization pattern which, as we will show, then evolves under mean-field dynamics into a soliton array.

The result of the phase winding procedure described above is demonstrated in Fig. 1. Fig. 1(a) presents a typical theoretical initial condition used subsequently for the simulation of the mean field dynamics, further described in the Supplemental Material [31]. The figure demonstrates the interpenetrating nature of the two atomic spin components together with the initial phase winding pattern projected onto the  $x$ - $y$  plane. Fig. 1(b) shows an experimental image for winding time  $\tau = 40$  ms. Two separate imaging light pulses were used to acquire an absorption image of atoms in the  $|2, -2\rangle$  state after 6 ms untrapped time-of-flight and in the  $|1, -1\rangle$  state after 7.5 ms. In the following, we will present only the images of the  $|2, -2\rangle$  state since the  $|1, -1\rangle$  state always exhibits a complementary structure.

The spatial periodicity of the produced pattern can be experimentally adjusted over a wide range by varying the winding time between the two microwave pulses.

The progression of the periodicity with increasing winding time is illustrated in Fig. 2(a) in  $k$ -space, where the Fourier spectra of the integrated cross-sections of the  $|2, -2\rangle$  state are shown. In Fig. 2(b), the position of the fundamental peak in  $k$ -space,  $k_0$ , as a function of the winding time indicates a winding rate of  $1.074(2) \mu\text{m}^{-1}\text{s}^{-1}$  for our magnetic environment. This implies a magnetic gradient of  $5.12(1) \text{ mG/cm}$  along the long axis of the BEC. Absorption images of the  $|2, -2\rangle$  component taken after  $\tau = 20$  ms, 60 ms and 100 ms are depicted in Figs. 2(c)-(e). In the experiment, we find that regular winding patterns can be produced for winding times up to  $\tau \approx 120$  ms, corresponding to  $k_0/2\pi = 0.1291(2) \mu\text{m}^{-1}$ , before the produced patterns become irregular.

**Numerical Method.** To monitor the dynamics of the DB soliton lattices we utilize the following system of coupled 3D Gross-Pitaevskii equations [8, 32]:

$$i\hbar\partial_t\Psi_j = \left( -\frac{\hbar^2}{2m}\nabla^2 + V(\mathbf{r}) + \sum_{k=1}^2 g_{jk}|\Psi_k|^2 \right) \Psi_j. \quad (1)$$

Here,  $g_{jk} = 4\pi\hbar^2 a_{jk} N_j/m$  with  $j = 1, 2$  indexing the relevant spin states,  $N_j = 3.5 \times 10^5$  is the particle number per component,  $a_{jk}$  are the 3D intra- ( $j = k$ ) and inter-component ( $j \neq k$ ) scattering lengths, and  $m$  is the mass of a  $^{87}\text{Rb}$  atom [31]. Additionally, the trapping potential  $V(\mathbf{r}) = \sum_{\xi=x,y,z} m\omega_\xi^2 \xi^2/2$  is characterized by the aforementioned experimental trapping frequencies whose aspect ratio leads to a cigar-shaped geometry.

To numerically initialize the dynamics, we first obtain the ground state of the interacting time-independent system of Eqs. (1). Then, we imprint on top of them the desired complementary configuration between the two components, with wave number  $k_0$  and a phase jump of  $\pi$  between adjacent domains, see also Fig. S1 and [31]. Subsequently, the resulting waveform is evolved in time.

**Time Evolution.** In the following, we focus on the time evolution of the soliton arrays after the end of the winding procedure. To establish a quantifiable measure of the soliton array dynamics with which to compare theory and experiment, we first compute the Fourier spectrum, as was done for Fig. 2(a). We then calculate the spectral power within one linewidth of the first ( $k_0$ ) and second harmonic peaks ( $k_1$ ) as determined from the initial state after the winding procedure [31]. The strength of these peaks provides a quantifiable measure of the regularity of the soliton array as well as the pattern contrast. The observed time evolution depends on the initial periodicity of the winding, leading to qualitatively different dynamical features for each winding regime.

First, we consider the dynamics near the optimally wound regime with a winding time  $\tau = 60$  ms (corresponding to  $k_0/2\pi = 0.07 \mu\text{m}^{-1}$ ) in Fig. 3, which showcases the most prototypical behavior of the system. In this case, a regularly spaced array of approximately

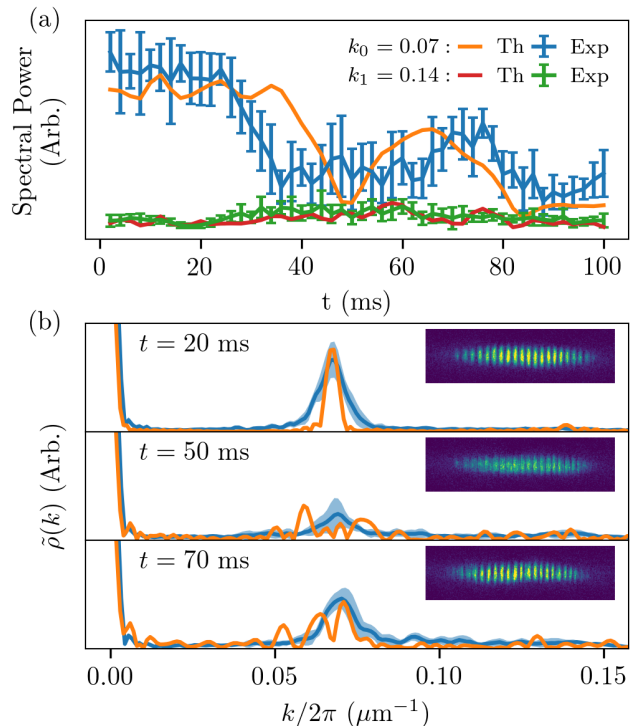


FIG. 3. (a) Evolution of the spectral power of the first ( $k_0$ ) and second harmonic peaks ( $k_1$ ) for  $\tau = 60$  ms. Each experimental point is an average over ten independent realizations with error bars representing one standard deviation. The 1D Fourier transforms are taken after integrating each absorption image along the transverse direction. (b) Experimental (blue line) and theoretical (orange line) Fourier spectra at select times. The shading around the experimental curve represents one standard deviation over ten realizations. The inset depicts a single-shot experimental image at each time.

twenty DB solitons is formed for our experimental parameters. Fig. 3(a) illustrates the evolution of the spectral power of the fundamental Fourier peak centered at  $k = k_0$  and the second harmonic peak centered at  $k = k_1$ . Fig. 3(b) presents the full spectrum averaged over ten independent experimental realizations for each time instant accompanied in each case by a relevant single-shot absorption image as an inset. For the first  $t = 20$  ms, the initial periodic structure robustly persists with no visible dynamics as captured by the nearly constant behavior of  $k_0$  shown in Fig. 3(a). Subsequently, a “sharpening” of the features is observed while the overall pattern periodicity remains unchanged. In the Fourier spectrum, this sharpening is indicated by the emergence of low amplitude higher harmonics, such as  $k_1$  in Fig. 3(a), while their peak positions are observed to remain fixed throughout the evolution. We attribute the onset of such dynamics to the fact that the initially generated winding pattern differs from the exact shape of a DB soliton lattice. Also, the intra- and intercomponent scattering lengths in the system are all very similar, but not exactly equal which



(see [31]) contributes to weakly miscible dynamics.

A peculiarity during the subsequent evolution is the emergence of a low-contrast regime which is most prominent in images taken within a time frame between  $t = 40$  ms and  $t = 60$  ms. Here, the pattern contrast in the experimental images has nearly or completely vanished. This is reflected in the Fourier spectrum in both theory and experiment by a strong decline in the amplitude of  $k_0$ , see Fig. 3(b) around  $t = 50$  ms. This decrease occurs faster in the experiment as compared to the theoretical prediction, which we attribute to the presence of a finite thermal fraction as well as the slight deviation between numerical and experimental initial conditions.

Remarkably, this evolution regime is followed by a revival of the periodic pattern with the same periodicity as the original pattern, shown in Fig. 3 around 70 ms. The fact that the system recovers its original periodic structure indicates a strong dynamical persistence of the soliton array and constitutes a key feature of our experimental and theoretical results. Eventually these dynamics lead to the loss of regularity of the pattern inside each BEC, which becomes pronounced for evolution times exceeding 80 ms.

The next case to be considered concerns the dynamical evolution of soliton arrays in the underwound regime where the characteristic size of a typical DB soliton is noticeably smaller than the length scale of the initial winding pattern. This case is realized e.g. with a winding time of  $\tau = 40$  ms, resulting in  $k_0/2\pi = 0.045 \mu\text{m}^{-1}$ . This regime leads to the spontaneous emergence of dark-antidark solitons [22, 30, 33], instead of DB solitons, which are characterized by the bright solitonic feature existing on top of a finite background. Dark-antidark solitons appear as a qualitatively new feature in our experiment (Fig. 4), which is also verified upon numerical integration of the 3D mean-field Eqs. (1) [31].

Monitoring the spectral power of the  $k_0$  peak in Fig. 4(a) for times up to  $t = 100$  ms reveals that the  $k_0$  peak diminishes as the  $k_1$  peak grows, in congruence with the formation of the dark-antidark soliton structures from the broader initial configuration. The persistence of the initial winding pattern is demonstrated in Fig. 4(a) by the high spectral power of the  $k_0$  peak for early times. The onset of antidark formation is captured by the appearance of right-shifted peak deformations in the integrated cross-section presented, e.g., in Fig. 4(c) at  $t = 34$  ms. The antidark soliton peaks move from the right to the left within each domain at later times, see Fig. 4(d) taken at  $t = 62$  ms.

The antidark solitons, consistently appearing in each experimental realization, emerge at the edges of each bright domain. Our numerical studies confirm the emergence of an array of dark-antidark solitons which, however, form at the center of the bright domains and do not experience drifts from right to left. We interpret this discrepancy as the result of a small, yet nonzero amount of

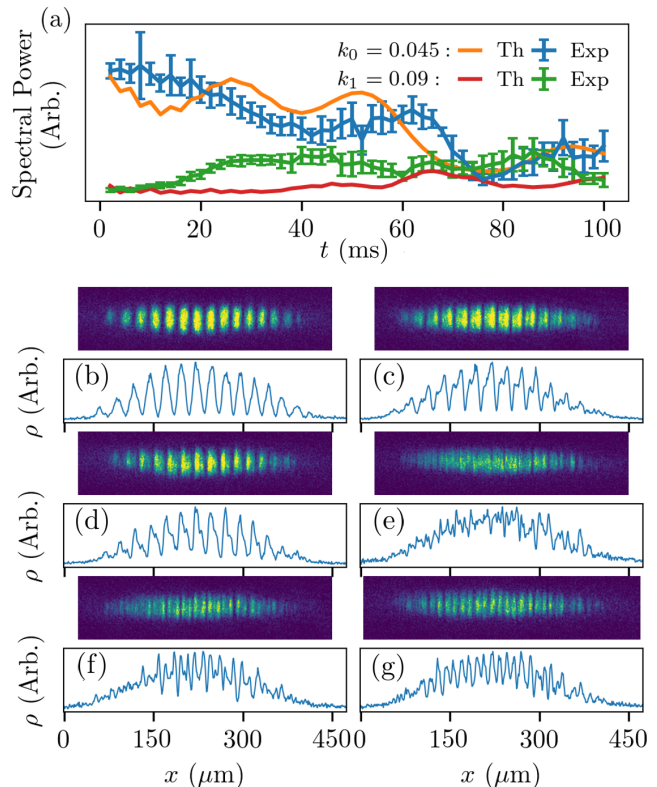


FIG. 4. (a) Time evolution of the spectral power of the significantly underwound case ( $\tau = 40$  ms). The experimental points are obtained after averaging the spectra of ten individual realizations of the experiment for each time step. (b)-(g) Stages in the evolution in the significantly underwound case: Single absorption images and their vertically integrated cross sections taken after evolution times of  $t = (2, 34, 62, 76, 78, \text{ and } 80)$  ms, respectively.

counterflow in the system produced by the initial winding procedure, which is not accounted for in the numerical simulations.

At  $t \approx 76$  ms, a low-contrast regime similar to the one described in the context of the  $\tau = 60$  ms case is observed in many iterations of the experiment; see, e.g., Fig. 4(e). The pattern contrast then partially recovers. Two peculiar observations in some images during the recovery and subsequent evolution include (i) the formation of peak/notch/peak features, reminiscent of dark-dark solitons [34, 35], corresponding to each original stripe (Fig. 4(f)), and (ii) the observation of images with an apparently doubled number of stripes (Fig. 4(g)) compared with the initial configuration (Fig. 4(b)). Correspondingly, in the Fourier spectrum the second harmonic peak  $k_1$  surpasses the near-vanishing  $k_0$  peak in this regime, as shown in Fig. 4(a) around  $t = 80$  ms, consistent with the observation of an apparent “soliton doubling”. The mean-field theory exhibits similar features identifying these observations of shape deformations of

the individual solitons. While the observation of the peak/notch/peak features is infrequent, the observation of the “doubled” pattern as in Fig. 4(g) is consistently reproduced.

Lastly, we consider an overwound configuration which features densely packed solitons. Fig. 2(e) shows an image of the structures generated with a winding time of  $\tau = 100$  ms, leading to an initial winding characterized by  $k_0 = 0.11 \mu\text{m}^{-1}$ . The periodicity of this configuration has a shorter length scale than the typical soliton length scale in this system, which leads to qualitatively different dynamics than the former cases. Here, the periodic structure persists for  $t \approx 20$  ms, giving way to disordered solitonic dynamics at longer time scales. The evolution is characterized in the Fourier spectrum by a gradual decrease in the amplitude of the peak at  $k_0$  and a growth of broad noise at lower  $k$  values. The pattern of solitons remains irregular for the remainder of the probed time evolution extending out to  $t = 100$  ms. Absorption images and detailed Fourier analysis of this tightly wound case are available in the Supplemental Material [31].

**Conclusions.** Our work reveals a surprising dynamical richness in the evolution of dense DB soliton arrays demonstrated through novel experimental realizations and numerical simulations. Depending on the density of the initial soliton patterns, the observed dynamics include: (i) the emergence of a low-contrast stage followed by a pronounced revival of the regular pattern, indicating the coherent evolution of the soliton array, (ii) an emergence of dark-antidark solitons in the underwound configuration (iii) the persistence of the soliton patterns for times up to and exceeding 100 ms and, finally, (iv) the observation of strong shape deformations of the solitary waves upon sufficiently long time evolution (including a near-splitting into two lobes). These features have been directly observed in our experimental images, and are also reflected in the Fourier analysis (which averages over numerous realizations) of the soliton arrays. The relevant features are qualitatively reproduced in our fully 3D numerical simulations.

We expect this work to provide a stepping stone towards a deeper exploration of multi-component soliton arrays and their properties. By making use of different atomic species with tunable interactions, together with analysis of lattice vibrational modes, the methods presented in this work could be extended to investigate the effect of crystal rigidity on soliton lattices. In particular, this may pave the way towards performing vibrational spectroscopy and extracting the relevant structure factors, and exploring the excitation spectra of soliton lattices. From a broader perspective, dense soliton arrays in BECs have the potential to provide insights into the strongly interacting regime of multiple coherent structures, affording an alternative perspective on superfluid crystal dynamics which is complementary to investigations of supersolids [36] in other contexts.

**Acknowledgements.** We acknowledge Maren Mossman for early contributions to the experimental investigation. S.M, T.B, and P.E. acknowledge funding from NSF through Grant No. PHY-1912540. S.I.M. acknowledges support from the NSF through a grant for ITAMP at Harvard University. This research was also supported in part by the National Science Foundation under Grant No. NSF PHY-1748958 (S.I.M and P.S.). This work (P.S.) has been funded by the Deutsche Forschungsgemeinschaft (DFG, German Research Foundation) – SFB-925 – project 170620586. This material is also based upon work supported by the US National Science Foundation under Grant No. PHY-2110030 (P.G.K.).

---

\* Email address: engels@wsu.edu

- [1] J. S. Russell, *The wave of translation in the oceans of water, air, and ether* (Triibner & Company, 1885).
- [2] D. J. Korteweg and G. De Vries, *The London, Edinburgh, and Dublin Philosophical Magazine and Journal of Science* **39**, 422 (1895).
- [3] Y. S. Kivshar and G. P. Agrawal, *Optical Solitons: From Fibers to Photonic Crystals* (Academic Press, 2003) pp. 1–540.
- [4] P. G. Kevrekidis, D. J. Frantzeskakis, and R. Carretero-González, *The Defocusing Nonlinear Schrödinger Equation* (SIAM, Philadelphia, 2015).
- [5] M. Kono and M. Skorić, *Nonlinear Physics of Plasmas* (Springer-Verlag, Heidelberg, 2010).
- [6] M. Ablowitz, *Nonlinear Dispersive Waves, Asymptotic Analysis and Solitons* (Cambridge University Press, Cambridge, 2011).
- [7] E. Infeld and G. Rowlands, *Nonlinear waves, solitons and chaos* (Cambridge University Press, Cambridge, 2000).
- [8] C. J. Pethick and H. Smith, *Bose-Einstein Condensation in Dilute Gases* (Cambridge University Press, Cambridge, United Kingdom, 2002).
- [9] L. Pitaevskii and S. Stringari, *Bose-Einstein condensation* (Oxford University Press, Oxford, 2003).
- [10] D. J. Frantzeskakis, *J. Phys. A: Math. and Th.* **43**, 213001 (2010).
- [11] F. K. Abdullaev, A. Gammal, A. M. Kamchatnov, and L. Tomio, *International Journal of Modern Physics B* **19**, 3415 (2005).
- [12] A. L. Fetter, *Rev. Mod. Phys.* **81**, 647 (2009).
- [13] S. Komineas, *Eur. Phys. J. Spec. Top.* **147**, 133 (2007).
- [14] Y. Kawaguchi and M. Ueda, *Phys. Rep.* **520**, 253 (2012).
- [15] D. M. Stamper-Kurn and M. Ueda, *Rev. Mod. Phys.* **85**, 1191 (2013).
- [16] P. Kevrekidis and D. Frantzeskakis, *Rev. Phys.* **1**, 140 (2016).
- [17] T. Bersano, V. Gokhroo, M. Khamehchi, J. D’Ambroise, D. Frantzeskakis, P. Engels, and P. Kevrekidis, *Phys. Rev. Lett.* **120**, 063202 (2018).
- [18] S. Lannig, C.-M. Schmied, M. Prüfer, P. Kunkel, R. Strohmaier, H. Strobel, T. Gasenzer, P. G. Kevrekidis, and M. K. Oberthaler, *Phys. Rev. Lett.* **125**, 170401 (2020).
- [19] X. Chai, D. Lao, K. Fujimoto, and C. Raman, *Phys. Rev. Research* **3**, L012003 (2021).

- [20] A. Farolfi, D. Trypogeorgos, C. Mordini, G. Lamporesi, and G. Ferrari, *Phys. Rev. Lett.* **125**, 030401 (2020).
- [21] K. Fujimoto, R. Hamazaki, and M. Ueda, *Phys. Rev. Lett.* **122**, 173001 (2019).
- [22] G. C. Katsimiga, S. I. Mistakidis, T. M. Bersano, M. K. H. Ome, S. M. Mossman, K. Mukherjee, P. Schmelcher, P. Engels, and P. G. Kevrekidis, *Phys. Rev. A* **102**, 023301 (2020).
- [23] B. Doyon, T. Yoshimura, and J.-S. Caux, *Phys. Rev. Lett.* **120**, 045301 (2018).
- [24] I. Redor, E. Barthélemy, H. Michallet, M. Onorato, and N. Mordant, *Phys. Rev. Lett.* **122**, 214502 (2019).
- [25] G. A. El, *Journal of Statistical Mechanics: Theory and Experiment* **2021**, 114001 (2021).
- [26] A. Schwache and F. Mitschke, *Phys. Rev. E* **55**, 7720 (1997).
- [27] A. Costa, A. R. Osborne, D. T. Resio, S. Alessio, E. Chrivi, E. Saggese, K. Bellomo, and C. E. Long, *Phys. Rev. Lett.* **113**, 108501 (2014).
- [28] W. Wang and P. G. Kevrekidis, *Phys. Rev. E* **91**, 032905 (2015).
- [29] C. Hamner, J. J. Chang, P. Engels, and M. A. Hoefer, *Phys. Rev. Lett.* **106** (2011), 10.1103/physrevlett.106.065302.
- [30] I. Danaïla, M. Khamehchi, V. Gokhroo, P. Engels, and P. Kevrekidis, *Phys. Rev. A* **94**, 053617 (2016).
- [31] See Supplemental Materials for additional details.
- [32] S. Stringari and L. Pitaevskii, *Bose–Einstein Condensation* (Oxford University Press, Oxford, United Kingdom, 2003).
- [33] H. Kiehn, S. I. Mistakidis, G. C. Katsimiga, and P. Schmelcher, *Phys. Rev. A* **100**, 023613 (2019).
- [34] M. A. Hoefer, J. J. Chang, C. Hamner, and P. Engels, *Phys. Rev. A* **84**, 041605 (2011).
- [35] D. Yan, J. J. Chang, C. Hamner, M. Hoefer, P. G. Kevrekidis, P. Engels, V. Achilleos, D. J. Frantzeskakis, and J. Cuevas, *J. Phys. B: At. Mol. and Opt. Phys.* **45**, 115301 (2012).
- [36] L. Chomaz, I. Ferrier-Barbut, F. Ferlaino, B. Laburthe-Tolra, B. L. Lev, and T. Pfau, *arXiv preprint arXiv:2201.02672* (2022), <https://doi.org/10.48550/arXiv.2201.02672>.
- [37] D. A. Steck, “Rubidium 87 d line data,” .
- [38] Personal correspondence with Servaas Kokkelmans (2017).
- [39] C. T. Kelley, *Solving nonlinear equations with Newton’s method* (SIAM, 2003).
- [40] P. Ao and S. T. Chui, *Phys. Rev. A* **58**, 4836 (1998).
- [41] S. I. Mistakidis, A. G. Volosniev, R. E. Barfknecht, T. Fogarty, T. Busch, A. Foerster, P. Schmelcher, and N. T. Zinner, *arXiv preprint arXiv:2202.11071* (2022), <https://doi.org/10.48550/arXiv.2202.11071>.

## Supplemental Material: “Dense dark-bright soliton arrays in a two-component Bose-Einstein condensate”

### EXPERIMENT CHARACTERIZATION

In this section, we provide a more complete description of the winding process described in the main text. We begin with an elongated BEC entirely in the  $|1, -1\rangle$  state, which we will refer to as spin up, with a magnetic bias field of 10 G in the vertical direction perpendicular to the long axis of the condensate. Here, it is helpful to consider a collection of Bloch spheres, one for each point along the long axis, as schematically illustrated in Fig. S1, with all Bloch vectors pointing up and in phase.

A near-resonant microwave pulse is tuned to coherently transfer half of the atomic population to the  $|2, -2\rangle$  state, which we will refer to as spin down, with a pulse time of approximately 0.1 ms. The pulse produces a uniform spin mixture across the condensate. Equivalently, this corresponds to a  $\pi/2$  rotation of the Bloch vectors, leaving them in phase along the equator of the Bloch sphere. Hence, we refer to this pulse protocol as a  $\pi/2$  pulse. The superposition state, shown in Fig. S1 on the second row, is then allowed to evolve in the optical trap during a variable amount of time, referred to as the winding time  $\tau$ .

During the winding time, each of the Bloch vectors precess at a different rate and adjacent Bloch vectors will acquire a phase difference proportional to their energy difference as  $\delta\phi = (\delta U/\hbar)t$ . In the single particle limit, this energy difference is given by the differential Zeeman splitting induced by a small gradient of the magnetic field strength along the long axis of the BEC. We take the energy to be locally linear in the magnetic field for small changes giving  $\delta\phi = \left(\frac{1}{\hbar} \frac{\partial U}{\partial B}\right)_{B=B_0} \Delta B t$ , where the variation in the energy between the  $|1, -1\rangle$  and  $|2, -2\rangle$  states of  $^{87}\text{Rb}$  at  $B_0 = 10$  G is 2.0972h MHz/G using the Breit-Rabi formalism [37]. The change in magnetic field between two points in the condensate can then be approximated by assuming that the gradient is linear along the long axis of the condensate, leading to  $\delta\phi = \left(\frac{1}{\hbar} \frac{\partial U}{\partial B}\right)_{B=B_0} \left(\frac{\partial B}{\partial x}\right) \Delta x t$ .

Finally, a second  $\pi/2$  pulse is applied which continues to rotate the Bloch vector about the same axis as the initial pulse. The last row of Fig. S1 shows how, depending on the acquired phase, the Bloch vectors will be unaffected, rotated back to the up state, rotated to the down state, or someplace in between along a sinusoidal pattern. When the phase difference between two points in the condensate is  $2\pi$ , both of those regions will be rotated in the same way by the final  $\pi/2$  pulse and thus represent a full wavelength of the final magnetization pattern – choosing  $\Delta x = \lambda$ , we identify the winding wavenumber

$$k_0(t) = \frac{2\pi}{\lambda} = \left(\frac{1}{\hbar} \frac{\partial U}{\partial B}\right)_{B=B_0} \left(\frac{\partial B}{\partial x}\right) t. \quad (\text{S1})$$

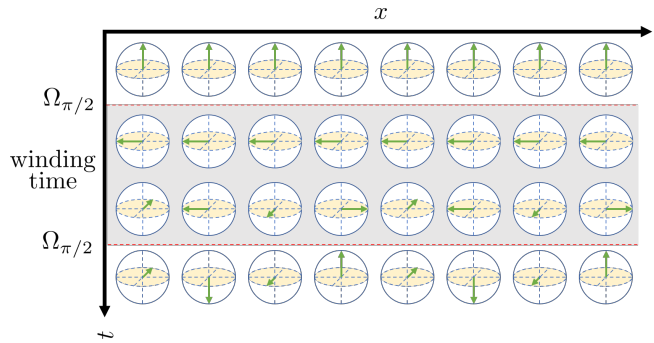


FIG. S1. Schematic of the winding process where position in the BEC is represented on the horizontal axis and time progresses downward. A microwave pulse rotates the Bloch vector into the equatorial plane which then precesses at an increasing rate from left to right due to a magnetic field gradient during the winding time, shown in grey. A second microwave pulse then rotates the Bloch vectors again depending on their orientation at the end of the winding time.

The slope extracted from Fig. 2(b) of the main text is the winding rate in Eq. (S1) from which the magnetic field gradient is obtained.

As each spin domain of the prepared magnetization pattern has undergone an additional phase rotation on the Bloch sphere relative to the adjacent domains, we would expect the condensate wave function to also acquire phase gradients of  $\pi$  across each winding. In the condensate picture, the effect of the small magnetic gradient during the winding time can be understood as a force which accelerates the spin-up and spin-down components in opposite directions. This acceleration results in a relative velocity corresponding to the phase difference in the condensate wave function between the two spin components. This phase difference then emerges as phase windings after the final  $\pi/2$  pulse remixes the two spin components, which then localize as phase jumps under mean field interactions to produce nearly stationary dark-bright solitons.

### ANALYSIS OF THE FOURIER TRANSFORM OF THE DENSITY

The primary quantitative measure of the periodicity of the DB soliton trains presented in this work is the spectral power obtained from the peaks in the Fourier transform of the density. From the single component absorption images, we see a periodic modulation of the density along the long axis of the condensate. We integrate the transverse direction to obtain a 1D cross section. During all experimental runs, some thermal fraction of atoms builds up due to various sources of heating – the ther-



mal fraction is extracted from the 1D cross section by fitting the atomic density to a Thomas-Fermi profile [9], fitting the portion of the cloud remaining outside of the Thomas-Fermi radius to a Gaussian, and then subtracting that Gaussian profile from the whole cross section. Each resulting cross section was checked for spurious fits until an adequately flat zero density background was obtained. Each cross section is then normalized to a fixed value before applying the fast Fourier transform (FFT) to obtain the spectral characteristics of the atomic density in  $k$ -space.

The Fourier spectra of the initial winding configurations are shown in Fig. 2(a) of the main text, showing a dominant peak corresponding to the periodicity of the winding and a smaller second harmonic feature. We observe that throughout the experimental observations of the subsequent time evolution, the central positions of the peaks in the FFT data (the wavenumbers  $k_i$ ) do not significantly change, i.e., these values are set during the winding procedure, and the time evolution is characterized by the change in strength of the FFT peaks and/or development of broadband noise. The regularity and contrast of the wound configuration at particular length scales can be quantified by the relative strength of the spectral power over fixed  $k$ -space ranges.

The spectral power is obtained in a systematic manner by fitting the fundamental spectral peak of the initial winding configuration with a Gaussian curve to obtain a line width  $\sigma$  in  $k$ -space. Then, the line width is used as limits of integration for the spectral power for all subsequent time slices, thus characterizing the spectral power of the periodic configuration within one  $\sigma$  of the central peak value  $k_0$ . This method allows one to compare the relative spectral power between  $k_0 - \sigma$  and  $k_0 + \sigma$  for both theory and experiment in a consistent way.

## MEAN-FIELD IMPLEMENTATION OF THE SOLITON ARRAYS

To numerically study the nonequilibrium dynamics of the dense DB soliton arrays we employ the dimensionless version of the 3D coupled Gross-Pitaevskii equations [17, 22] provided in the main text, see also Eq. (1). As such, the underlying particle ( $N_1 = N_2 = N/2 = 3.5 \times 10^5$ ) and mass ( $m_1 = m_2 = m$ ) balanced  $^{87}\text{Rb}$  mixture is described by

$$\begin{aligned} i\partial_t\Phi_1(t) &= -\frac{1}{2}\nabla^2\Phi_1(t) + V(\mathbf{r})\Phi_1(t) \\ &+ (4\pi a_{1,1}N_1|\Phi_1(t)|^2 + 4\pi a_{1,2}N_2|\Phi_2(t)|^2)\Phi_1(t), \\ i\partial_t\Phi_2(t) &= -\frac{1}{2}\nabla^2\Phi_2(t) + V(\mathbf{r})\Phi_2(t) \\ &+ (4\pi a_{2,1}N_1|\Phi_1(t)|^2 + 4\pi a_{2,2}N_2|\Phi_2(t)|^2)\Phi_2(t), \end{aligned} \quad (\text{S2})$$

Here, the Laplacian operator is  $\nabla^2 \equiv \partial_x^2 + \partial_y^2 + \partial_z^2$ , whilst the employed 3D scattering lengths for  $^{87}\text{Rb}$

are  $a_{1,1} = 100.40(10)$ ,  $a_{2,2} = 98.98(4)$ , and  $a_{1,2} = 98.98(4)$  in units of the Bohr radius  $a_0$  [38]. State 1 is  $|F, m_F\rangle = |1, -1\rangle$ , state 2 is  $|2, -2\rangle$ , and  $m$  is the mass of  $^{87}\text{Rb}$ . The dimensionless 3D parabolic external potential reads  $V(\mathbf{r}) = \frac{1}{2}\omega_x^2(x^2 + (\omega_y/\omega_x)^2 y^2 + (\omega_z/\omega_x)^2 z^2)$  with  $\mathbf{r} = (x, y, z)$ . Following the experimental implementation the axial and transverse trapping frequencies are  $(\omega_x, \omega_y, \omega_z) = 2\pi \times (3.06, 267, 278)\text{Hz}$  justifying a highly-elongated (cigar-shaped) geometry possessing an aspect ratio  $\omega_x/\omega_y \approx \omega_x/\omega_z \approx 0.01$ .

Moreover, the rescaling used for the spatial and temporal coordinates is  $x' = a_{\text{ho}}^{-1}x$ ,  $y' = a_{\text{ho}}^{-1}y$ ,  $z' = a_{\text{ho}}^{-1}z$ , with  $a_{\text{ho}} = \sqrt{\hbar/m\omega_x}$  denoting the harmonic oscillator length along the longitudinal  $x$ -direction, and  $t' = \omega_x t$ , respectively. Accordingly, the wave function of each hyperfine state ( $j = 1, 2$ ) is rescaled as  $\Phi_j(x', y', z') = \sqrt{N_j/a_{\text{ho}}^3}\Psi_j(x, y, z)$  and the Laplacian is rescaled as  $\nabla_{r'}^2 = a_{\text{ho}}^2\nabla^2$ .

To emulate the experimental preparation we first obtain the ground state of the fully interacting 3D binary setting utilizing a fixed point iterative scheme of the Newton type [39]. Since the interactions lie close to the miscibility/immiscibility threshold ( $a_{1,2}^2 \approx a_{1,1}a_{2,2}$ ) [40, 41] but slightly on the miscible side, the ground state wave functions of the individual components are spatially miscible while the total density has a Thomas-Fermi profile. As a subsequent step, we craft on top of the aforementioned ground states the following sinusoidal ansatz (see Fig. 1(a) in the main text)

$$\tilde{\Phi}_1(x, y, z) = \sqrt{\cos^2(kx)}\Phi_1(x, y, z; 0) e^{i\pi \cos(kx/2)}, \quad (\text{S3})$$

$$\tilde{\Phi}_2(x, y, z) = \sqrt{\sin^2(kx)}\Phi_2(x, y, z; 0) e^{i\pi \cos(\pi/4+kx/2)}, \quad (\text{S4})$$

where  $\Phi_j(x, y, z; 0)$  is the ground state of each component at  $t = 0$ . Notice that these crafted wave functions of the two components along the longitudinal  $x$ -direction are complementary with respect to one another. An almost perfect total Thomas-Fermi density profile occurs in the decoupled case with weak spatial undulations appearing for increasing (principal) wavenumbers  $k = k_0/(2\pi)$  illustrated in Figs. 2(a) and 2(b) of the main text. Finite intercomponent interactions for a fixed  $k_0$  lead to more pronounced spatial undulations. Subsequently, we let the above system dynamically evolve for times up to  $t = 100\text{ms}$ . The spatiotemporal evolution of the two-component bosonic system is captured using a fourth-order (in time) Runge-Kutta method characterized by temporal and spatial discretization  $dt = 10^{-4}$  and  $dx = 0.03$ ,  $dy = dz = 0.05$  respectively. Also, a second order finite difference scheme is employed to resolve the spatial derivatives.



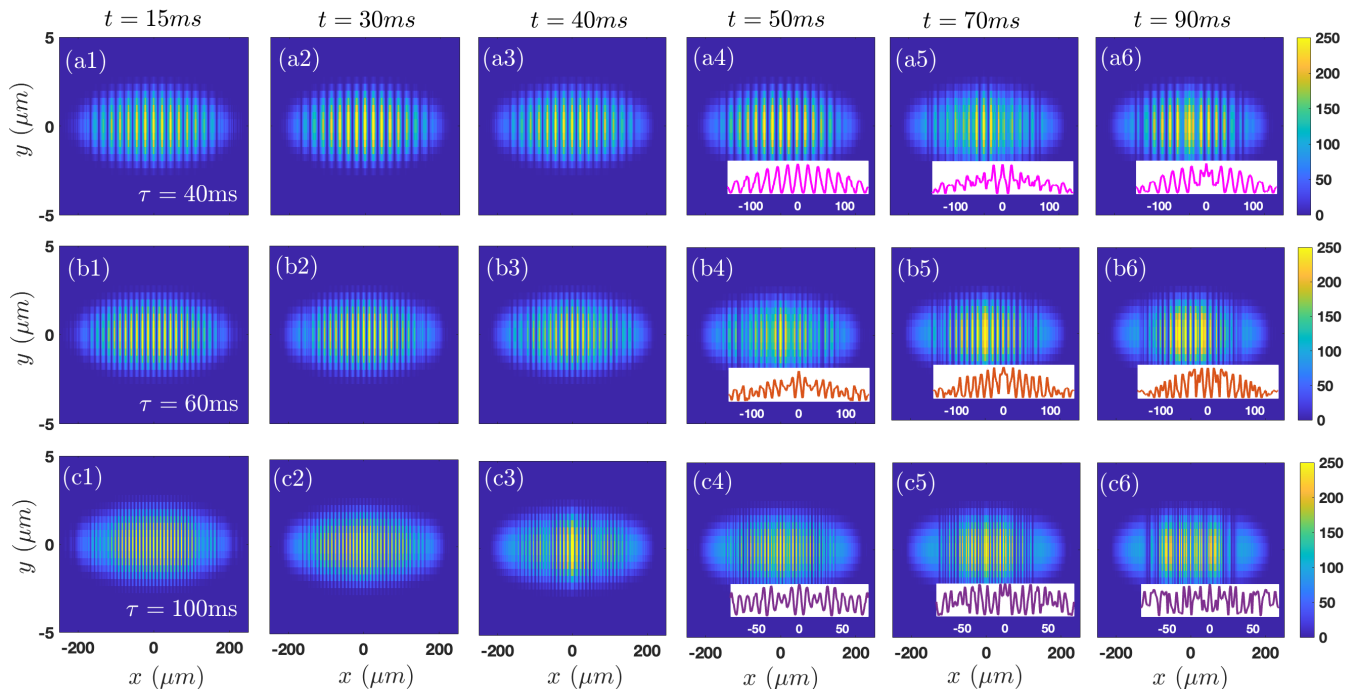


FIG. S2. Numerically calculated density snapshots for (a1)–(a6)  $\tau = 40$ ms, (b1)–(b6)  $\tau = 60$ ms, (c1)–(c6)  $\tau = 100$ ms windings. In all cases, only one component is visualized since the second is complementary to it. Insets depict the integrated along the  $y - z$  plane density profiles; notice the different scale in each inset, selected for better visualization. Progressively antidark structures develop for  $\tau = 40$ ms; see e.g. the dynamics close to the center. The initial soliton array at  $\tau = 60$  ms loses its contrast around  $t = 50$ ms and a recurrence of the pattern takes place at later times. In the  $\tau = 100$ ms scenario the coherence of the initial DB soliton array is lost in the course of the evolution due to interactions.

### FURTHER DYNAMICAL FEATURES OF THE SOLITON ARRAYS

Characteristic density profiles during the nonequilibrium dynamics of the 3D system of coupled GPEs [Eq. (S2)] are presented in Fig. S2 for the three winding protocols discussed in the main text, namely for  $\tau = 40$  ms, 60 ms, and 100 ms. Particularly, Fig. S2(a1)–(a6), show the underwound configuration for  $\tau = 40$  ms. The selected time instants correspond to the dynamical region where  $k_0$  possesses a high [Fig. S2(a1)], moderate [Fig. S2(a2)], and lower [Fig. S2(a3)] intensity as captured by the spectral power illustrated in Fig. 4(a) of the main text. In this time interval an ordered soliton array is observed persisting also for later times, see Fig. S2(a4) and the integrated density profile depicted as an inset. Recall that a similar dynamical pattern is seen in the experimental cross section e.g. of Fig. 4(b). Such an ordered pattern remains robust until the substantial descent of  $k_0$ 's intensity occurring approximately for  $t > 60$  ms. The descent of  $k_0$ 's intensity signifies the spontaneous emergence of dark-antidark soliton arrays, see Fig. S2(a5), (a6) and their relevant insets especially around the trap center.

Turning to the optimally wound scenario,  $\tau = 60$  ms,

it is found that the regularity of the soliton array is slightly distorted sooner than in the  $\tau = 40$  ms case, compare Fig. S2(a1)–(a3) with Fig. S2(b1)–(b3). A lower contrast region occurs at later evolution times [see e.g. Fig. S2(b4)] followed by a recurrence tendency towards the original array where solitons are equally spaced and regularly ordered [Fig. S2(b5), (b6)] in accordance with the experimental observations.

Finally, Fig. S2(c1)–(c6) demonstrates the dynamical evolution of an overwound configuration, prepared in the experiment with winding time  $\tau = 100$  ms. Notice that a regular highly dense soliton array occurs at initial times [Fig. S2(c1)] but this regularity is soon lost as it is shown e.g. for  $t = 30$  ms [Fig. S2(c2)] and  $t = 40$  ms [Fig. S2(c3)]. Progressively, even more irregular soliton patterns are evidenced, persisting in such a disordered arrangement for evolution times up to  $t = 100$  ms [see Fig. S2(c4)–(c6) and the corresponding integrated density profiles provided as insets]. Fig. S3 shows detailed results for the overwound case discussed above and described in the main text. Panels of Fig. S3(a)–(d) demonstrate the FFT results for the time progression as the ordered array decays into a disordered collection of solitons at times  $t = 0$  ms, 5 ms, 8 ms, and 10 ms. We observe that as the primary spectral peak  $k_0$  decays, broadband noise develops for  $k < k_0$

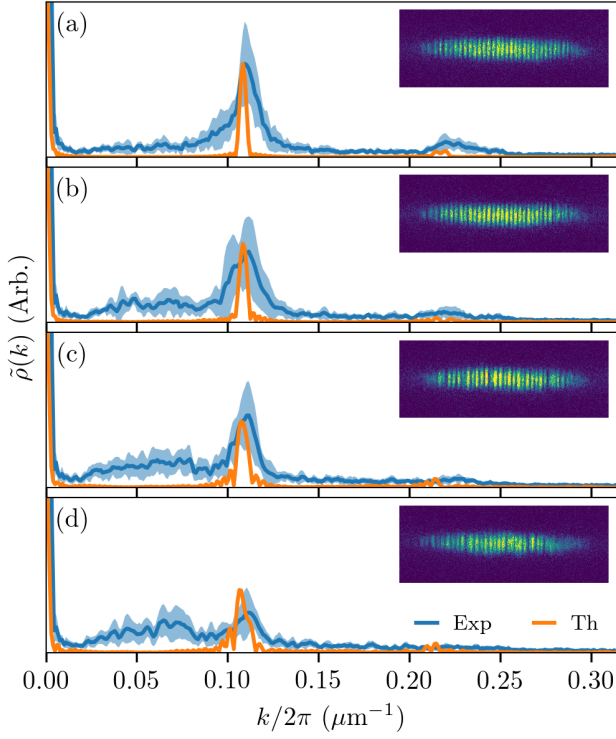


FIG. S3. Time evolution after 100 ms winding. (a)-(d) Fourier transform of the density for evolution times  $t = 0$  ms, 5 ms, 8 ms, and 10 ms, respectively, with a representative absorption image inset for each. Experimental data averaged over ten realizations is drawn in blue with shading representing one standard deviation. The Fourier transforms of the corresponding theory realizations are shown in orange.

indicating disordered dynamics of a longer length scale than the initially formed solitons. For each time segment an inset is provided with an example of an experimental absorption image to identify the qualitative nature of the soliton dynamics. The character of the experimental observations shown in Fig. S3 persists through the rest of the experimentally probed time, up to  $t = 100$  ms, where we observe that the solitons do not decay but also do not remain in an ordered array. The theory curves are illustrated for comparison – while the aforementioned 3D GPE predictions capture the same qualitative behavior, the decay into the disordered array occurs at later time intervals.